



Structural and Optical Properties of CeO₂ Nanoparticles Synthesized by Modified Polymer Complex Method

Jazmín Calvache-Muñoz¹ · Fabiola A. Prado¹ · Liliana Tirado² · Lucy Caterine Daza-Gomez³ · Germán Cuervo-Ochoa⁴ · Heidy L. Calambas⁵ · Jorge E. Rodríguez-Páez¹

Received: 4 September 2018 / Accepted: 13 December 2018 / Published online: 2 January 2019
© Springer Science+Business Media, LLC, part of Springer Nature 2019

Abstract

Ceria nanoparticles (Ceria-NPs) were synthesized using a modified polymer complex method and their structural and optical properties were evaluated. The solids were heated at 550 °C and characterized using Raman, UV–Vis absorption, diffuse reflectance, X-ray photoelectron and photoluminescence spectroscopies, X-ray diffraction (XRD) and scanning and transmission electron microscopy. The primary particles obtained presented a size of ~10 nm. The XRD indicated that CeO₂ was the only crystalline phase. From the UV–Vis and diffuse reflectance spectra, energy values of 3.8 eV and 3.4 eV were obtained, values that can be associated with band–band electronic transitions and/or with those that involve ionized states located within the gap caused by defects and isolated atoms of Ce³⁺. Photoluminescence spectra reiterated the existence of localized states in the gap. Raman spectra revealed the existence of peroxide (O₂²⁻) and superoxide (O₂⁻) over the surface of the ceria-NPs. The XPS results indicated that the concentrations of Ce³⁺ and Ce⁴⁺ were ~20.5% and ~79.5% respectively, and that the stoichiometry of oxygen was 1.9 per atom of Ce. The results obtained from the characterization of CeO₂-NPs synthesized make it as promising material for environmental remediation, biomedicine, gas sensing and optoelectronic applications.

Keywords Ceria-NPs · Synthesis · Modified polymer complex · Structural properties · Optical properties

1 Introduction

Pure cerium oxide has a fluorite type structure, with a *Fm3m* spatial group, a structure that is maintained between ambient temperature and its melting point. Cerium oxide has at least two stoichiometrically stable forms—dioxide (CeO₂) and dicerium trioxide (Ce₂O₃), commonly known as sesquioxide [1, 2]. The phase transition CeO₂ ↔ Ce₂O₃ is influenced by the conditions of pressure of oxygen and temperature of

the medium [1], a transition of reduction that is explained taking into account the formation and migration of oxygen vacancies. This transition may be related to a quantum process of ionization/delocalization of the cerium 4f electrons, as Skorodumova et al. proposed [3], where there would be a simultaneous capture of two electrons into localized f-level traps on two cerium atoms. Such oxygen vacancies could be considered as the major factor for storing oxygen in ceria [4] and their formation produces a rise in the Ce³⁺ fraction in the structure of the ceria in order to maintain its electro-neutrality [5]. Due to the close thermal stability of the CeO₂ and Ce₂O₃, an easy reversible transition between these compounds is favored, fostering, in addition, a range of partially-reduced CeO_{2-x} phases that can be viewed as a formation, migration and ordering of virtual Ce³⁺ vacancy complexes [3, 6]. The possible existence of these intermediate phases has motivated their study, more so when considering the technological developments they can bring [6], using the capacity ceria has for oxygen storage. As mentioned previously, it is expected that the valence and structural defects of the CeO₂ be dynamic characteristics of the solid and that these be affected by temperature, oxygen partial pressure,

✉ Jorge E. Rodríguez-Páez
jnpaez@unicauca.edu.co

¹ CYTEMAC Research Group, Department of Physics, University of Cauca, Popayan, Colombia
² Optoelectronic Group, Interdisciplinary Institute of Science, University of Quindío, Armenia, Colombia
³ Chemical Sciences, Autonomous University of Mexico, Mexico City, USA
⁴ GIPEL Group, Department of Chemistry, University of Cauca, Popayan, Colombia
⁵ GIDEMP Group, Biotechnology and Nanotechnology Line, Tecnoparque – SENA ASTIN, Cali, Colombia

doping with other ions, application of an electric field, or surface stress [2].

Looking at the optical properties of the semiconductor particulates, in this case ceria-NPs, consideration must be given to the evolution of the properties of the matter from atoms (discrete energy states) through to crystals (energy bands), modifications that can be described in terms of two stages: from atom to cluster and from cluster to crystal [7]. When the size of the particle grows, the properties can be described in terms of the size and morphology of the particle. From the point of view of the solid state, nanoparticles are a type of structure of low dimensionality where translational symmetry has been totally broken and only a finite number of electrons and holes can be created in the inside. Furthermore, the finite number of atoms in NPs can promote a variety of persisting photo-induced, photo-physical and photo-chemical phenomena that cannot occur in the solids. Thus, NPs can present inhomogeneous wide spectra, concentration defects, fluctuation forms, etc. These have provided the motivation for a systematic study of the optical properties of semiconductor NPs, stimulated by the development of quantum confinement approximation and properties that stem from this condition. As for all materials, the characteristics of the electronic structure of cerium oxide define all of its optical properties [8].

In Fangxin et al. [9], the results are shown of ultraviolet–visible (UV–Vis) optical reflectivity of nano-crystalline ceria with various particle sizes and the analysis of the mechanisms of the optical absorption and the optical reflectivity. These researchers suggest an intermediate band at 4.2 eV between the O_{2p} valence band and the Ce_{5d} conduction band, which involves charge transition from the O_{2p} valence band to the Ce_{4f} localization band. Recently Nikolic et al. [10] showed that the optical characteristics of ceria depend on the method of synthesis. The results of UV–Vis reflectance spectra indicated different band gap values. This was explained by taking into account structural imperfections in both particle core and surface. Partial reduction of the cerium ions, with the corresponding creation of oxygen vacancies, would lead to the introduction of energy levels in the gap and therefore smaller gap values.

Due to the characteristics of ceria, among them the capacity to store and liberate oxygen through the facility of forming and repairing oxygen vacancies on its surface, mainly [11], this oxide presents a broad range of technological applications. These special properties of ceria have promoted its use in the area of catalysis [12, 13], the production and purification of hydrogen [14], and the removal of CO [15], as well as electrolyte for solid oxide fuel cells [16]. Due to its electronic structure, ceria can be used as a UV absorber in the cosmetics industry as well as optical display [17]. Moreover, CeO_2 is employed in the treatment of toxic emissions, the removal of soot from diesel engine exhaust

and organic molecules from wastewater [18], in biomedicine [19], as oxygen sensor [20], in pharmacology [21] and dye degradation [22].

Ceria has traditionally been obtained using a wide variety of methods [23–29] and it has been found that the process of synthesis determines its properties and therefore its potential uses [23]. Specifically, nanoparticles of CeO_2 (CeO_2 -NPs) have a higher chemical activity due to the formation of oxygen vacancies and to the increase of the surface-to-bulk ratio [23, 30]. This is why researchers are studying synthesis processes that allow control of the size and morphology of the ceria [13, 23, 24, 31], using the surfactant [32, 33] and controlling parameters of synthesis such as temperature [34], acid–base nature of the system [35], and solvent type [36], among others. Controlling the synthesis process would make it possible to manipulate the morphology and size of the ceria particles [37], as well as of other properties of the end product, which would ultimately define its potential technological applications. Yuan et al. [37] demonstrate the interest that exists in determining the effect of synthesis parameters on the shape and the size of the particles obtained, and the high sensitivity that the process has to the nature of the solvent and/or the surfactant, pH gradients, environmental conditions (temperatures, pressure and humidity), pollutants, time, etc.

In the present work, ceria-NPs were synthesized using a modified polymer complex (PC) process, a method that enabled ceria-NPs with a high chemical purity to be obtained in a controlled and reproducible way at low temperatures. This method has several advantages such as its low cost and its low-temperature operation; it is a simple method, with controllable parameters, and homogeneous blending at the molecular level [38]. The basic idea of the PC method is to reduce individualities of the different metal ions, which can be achieved by encircling stable metal-chelate complexes steadily by a growing polymer net. Immobilization of the metal-chelate complexes in that rigid organic polymer net reduces the segregation of particulate metals during the process of decomposition of the polymer at moderate temperatures. In contrast to the previous study [39], which dealt with the mechanism of formation of the CeO_2 particles, in the current work the optical and structural properties of the synthesized CeO_2 -NPs were analyzed, in light of their potential applications. To do this, the solids obtained were characterized using X-ray diffraction (XRD), scanning (SEM) and transmission electron microscopy (TEM) and Raman and XPS spectroscopies. To understand their optical properties, UV–Vis absorption and diffuse reflectance spectroscopies were used, as well as photoluminescence.

2 Materials and Methods

2.1 Synthesis of Cerium Oxide

To obtain the ceramic powder of the CeO_2 system the modified polymer complex method was used, as indicated in a previous article [39]. Hydrated cerium nitrate ($\text{Ce}(\text{NO}_3)_3 \cdot 6\text{H}_2\text{O}$ —Alfa Aesar, 99.5%) was used as precursor in a mixture of citric acid (CA—Merck 99.5%) and ethylene glycol (EG—Mallinckrodt 99.8%), in a 1:4 mass ratio. The mixture was heated at 100 °C under continuous stirring and then brought to ambient temperature and the precursor added, maintaining stirring of the system to ensure a homogeneous mixture. Ammonium hydroxide (NH_4OH —Merck 25%) was then added to the obtained solution using a dispenser (Metrohm Dosimat 685) and the system was brought to the working pH, ensuring that the solution remained clear; simultaneously, water was added gradually until a total volume of 220 mL was obtained, independent of the working pH value. To remove the agglomerates present in the mixture, it was subjected to the action of high-shear equipment (Ultraturrax T50). The

solution was then heat treated at 150 °C for 3 h under constant stirring, to favor the formation of the resin.

On obtaining the resin, it was subjected to a pre-calcination process at 350 °C in an oven (Haceb HL40) for 2 h. After macerating the resulting solid, a light-yellow powder was obtained. This powder was treated at 550 °C, for 3 h, to completely remove the organic phase present in the sample. In Fig. 1 a diagram of the synthesis method used to obtain the CeO_2 -NPs is shown.

In summary, the parameters of the synthesis process that were analyzed were, mainly, the pH of synthesis (working pH) and the heat treatments, temperature and duration of the treatment. The total number of samples analyzed was 17.

2.2 Characterization of the Ceramic Powder

To determine the characteristics of the synthesized solids, various characterization techniques were employed.

2.2.1 Structural and Morphological Characterization

To determine the crystalline phases present in the samples of ceria synthesized, at different values of pH and heated

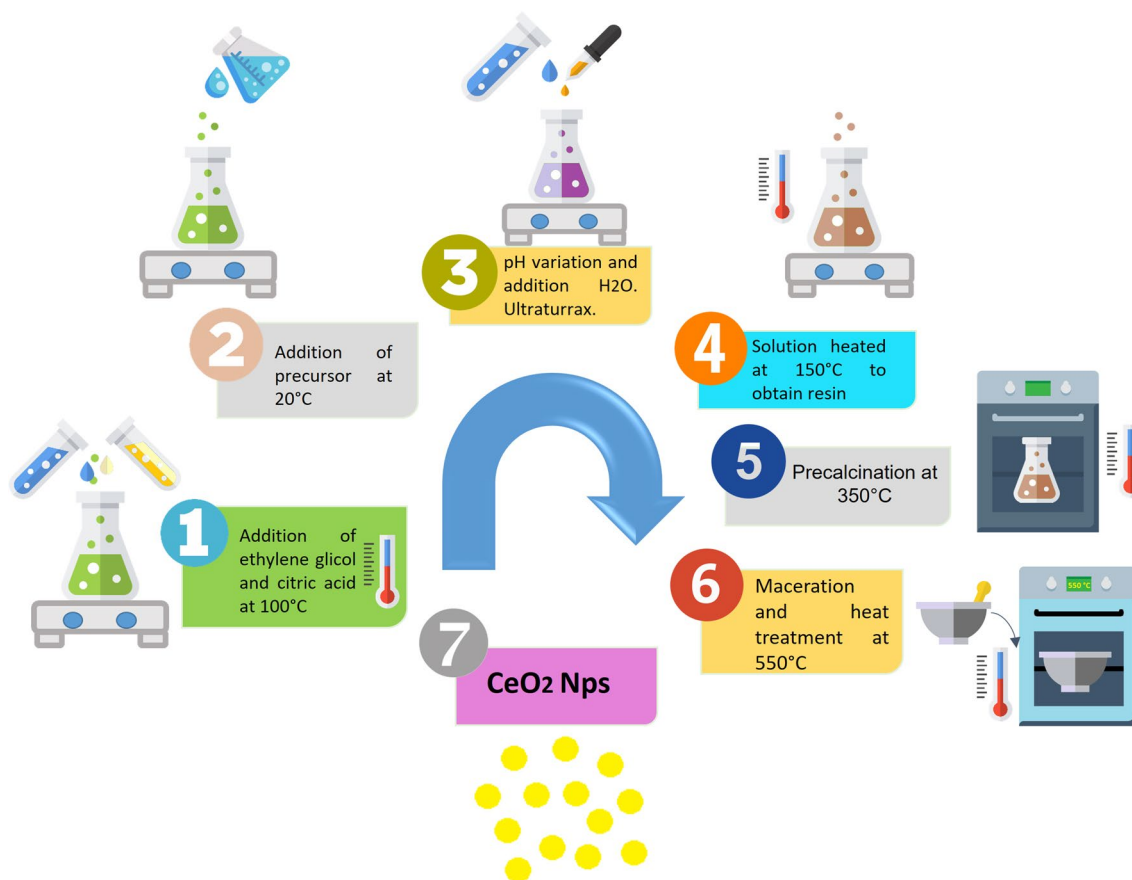


Fig. 1 Diagram of synthesis process used to obtain the cerium dioxide nanoparticles

at 550 °C for 3 h, X-ray diffraction (XRD) was used. For this purpose, the X-ray diffractometer (Pro PANalytical X'Pert X-ray) was used employed radiation K_{α} of Cu ($\lambda = 1.5418740 \text{ \AA}$). The powdered samples were analyzed in a range between 20° and 100°, with a step of 0.004 and a time per pass of 90 s.

In this work, TEM and SEM were used to determine the size and morphology of the particles in the samples obtained, using the Jeol JEM-1200EX electron microscope and the EVO MA10, Carl Zeiss—SEM spectrometer. The samples used for TEM observation were prepared by dispersing the synthesized powder in ethanol, followed by ultrasonic vibration for 30 min, then placing a drop of the dispersion onto a copper grid.

Raman spectroscopy is a powerful method for investigating disordered structures and crystal defects. For this, the Raman spectra of the samples of ceria synthesized were taken. The Thermo Scientific DXR SmartRaman spectrometer, equipped with a laser of 780 nm, with a spatial resolution in the range of 80–3500 cm^{-1} , was used. Raman scattering measurements were performed at room temperature on powders pressed into pellets.

2.2.2 Optical Characterization

The UV–Vis absorption spectra of the synthesized cerium oxide samples were taken with the Thermo Scientific Genesys 6 UV–Vis, in a wavelength range of 200–900 nm, using quartz cuvettes of 1 cm in length. To do this, 2.0 mg were taken of the synthesized ceria powder, previously macerated in an agate mortar, which was dispersed in 20 mL of distilled water. Absorption spectrum of this suspension was then taken. To be able to determine the contribution of the different electronic transitions of the synthesized ceria, such as the interband transitions related to the gap, the transitions between orbitals localized on the ions (charge interchange), the contribution of the defects, etc., deconvolution was performed on the UV–Vis spectra, using the Voigt A function with Fityk software. Complex models or functions are often the result of the sum of many functions. F is constructed as a list of component functions and is computed as $F = \sum_i f_i$.

Diffuse reflectance ultraviolet–visible spectroscopy was used to obtain the energy gap value of the ceria samples synthesized. The diffuse reflectance spectra of the predetermined samples were recorded using the Jasco V-670 UV–Vis–NIR spectrophotometer, in the wavelength range of 200 to 800 nm, at a scanning speed of 100 nm/min.

The photoluminescence (PL) spectroscopy study was done using as excitation source the 488 nm ($\sim 2.5 \text{ eV}$) line of an Ar^+ laser, with an LP540 filter at a power of 40 mW and its spectrum was analyzed with a spectrometer of 0.5 m focal distance and a range of 500–900 nm. For the detection

of the response, a photomultiplier tube was used, linked to a phase-sensitive “lock-in”. This set-up allowed the study, in more detail, of the transitions that the defect states involve, because with the laser used to excite the electrons, it was not possible to promote transitions between bands. To understand the latter, a Xenon Laser was used at a wavelength of 360 nm ($\sim 3.5 \text{ eV}$), along with a Horiba FluoroMax 4 spectrometer.

2.2.3 Surface Characterization: X-ray Photoelectron Spectra (XPS)

XPS is a straightforward, non-destructive technique for the investigation of the chemical and electronic structure of materials [40, 41]. An important advantage of XPS is its ability to identify binding and associated oxidation states of cerium in the CeO_2 -NPs. X-ray photoelectron spectra (XPS) of the CeO_2 -NPs synthesized at pH 9.1 were collected using a SPECS system equipped with a Phoibos 150 2D-DLD elevated pressure energy analyzer, installed in a high-vacuum chamber with the base pressure below 10^{-8} mbar. The X-ray excitation was provided by Al K_{α} radiation with photon energy $h\nu = 1486.6 \text{ eV}$ and at a power of 200 W. The spectra were collected at the pass energy of 60 eV in the fixed analyzer transmission mode. Surface charge compensation was carried out using a Flood Gun (FG 15/40-PS FG500) operated at 70 μA –2 eV. The powder under analysis was dusted onto an adhesive carbon tape.

The XPS spectrum corresponding to the CeO_2 -NPs synthesized at pH 9.1 was used to determine the relative concentrations of the Ce^{3+} and Ce^{4+} cations from the Ce $3d_{5/2}$ line. To do this, the spectrum background was subtracted using the Shirley approximation to remove the contribution of the inelastically scattered photoelectrons. The Ce 3d level was then deconvoluted using Gaussian–Lorentzian peak fitting and the spectra analyzed using the CasaXPS program (Casa Software Ltd), using the SPECS Prodigy-ACenteno library equipped with R.S.F. values (Response Sensitivity Factor) determined by the manufacturer. The relative atomic concentrations of the Ce^{3+} and Ce^{4+} cations were determined as the ratio of the respective peak areas (i.e. the total area of the peaks assigned to the Ce^{4+} component and the total area of the peaks assigned to the Ce^{3+} component).

3 Results and Discussion

3.1 Synthesis Process

The diagram in Fig. 1 describes the different steps of the ceria nanoparticle synthesis process using the Pechini polymer complex method. In reference [39] a detailed description

is given of the mechanism of formation of ceria nanoparticles using this synthesis process.

3.2 Results of Characterization of Ceria Samples Synthesized

3.2.1 Crystalline Structure of the Synthesized Ceria

When the synthesized samples were subjected to a heat treatment at 550 °C/3 h, a yellow powder characteristic of ceria was obtained. Figure 2a shows the X-ray diffractograms corresponding to the synthesized powder at different pH values and treated at 550 °C/3 h.

In Fig. 2a diffraction peaks can be seen that are well defined and correspond to the cubic fluorite type structure (JCPDS 34-0394). The lattice parameters obtained using Rietveld refinement (MAUD program), for the different samples synthesized, were as follows: 5.4093 Å (CeO₂ obtained at pH ~ 1); 5.4140 Å (CeO₂ obtained at pH 2.0), a value close to the standard 5.4113 Å (JCPDS 34-0394), and 5.392 Å for the sample synthesized at pH ~ 9.1.

The crystal size of each of the synthesized samples was also determined, using the Scherrer equation given by:

$$\tau = \frac{K\lambda}{\beta \cos\theta} \quad (1)$$

where τ is the mean crystallite size, K is a dimensionless form factor (in this work the value of 0.9 was used), λ is the wavelength of the incident X-rays, β the width at the mean peak height (FWMH) and θ the diffraction angle. The calculations made demonstrated that the crystal sizes had values of: 12.5 nm (synthesis pH ~ 1), 14.2 nm (pH ~ 2.0) and 12.4 nm (pH ~ 9.1).

3.2.2 Transmission and Scanning Electron Microscopy: Morphology and Particles Size

Figure 2b and c shows TEM and SEM images, respectively, of ceria synthesized at different synthesis pH values. Although the sample analyzed was previously subjected to ultrasound, the electron microscope images show high agglomeration (Fig. 2b and c). The sample synthesized at pH ~ 9.1 (Fig. 2b and c) meanwhile showed the smallest size of primary particle, between 10 and 20 nm taking as reference the scale of the photograph, and a spheroidal morphology.

3.2.3 UV–Vis Absorption Spectra of the Cerium Oxide Synthesized

Figure 3a shows the UV–Vis absorption spectra corresponding to the commercial ceria (SIGMA 99.9%) and to the samples synthesized in this work (treated at 550 °C/3 h). In these absorption spectra a wide band

stands out between 250 and 400 nm, with a maximum at 337 nm. The deconvolutions of the UV–Vis spectra in Fig. 3a-i are shown in Fig. 3a-ii to a-v. In these the presence is highlighted of three important bands for which the energy value associated with the corresponding electronic transition was determined, using the equation $E = \frac{h.c}{\lambda}$. Table 1 shows the values obtained when these calculations are carried out.

In CeO₂, as in semiconductors, the absorption of photons with the same energy or superior in the band gap generates electron–hole pairs. In this work, photons with lower energies than the inter-band transition energy were observed, as is shown in Fig. 3a and indicated in Table 1, which indicates the presence of ionized states within the gap, associated with the defects, and the existence of a large amount of defects in the ceria. The deconvolutions of the UV–Vis absorption spectra of the synthesized nanoparticles (Fig. 3a) present three important bands located at ~ 212, ~ 329 and ~ 358 nm, with energy values of 5.8, 3.8 and 3.4 eV respectively. The energy gap between the occupied 2p band of O and unoccupied band of 5d and 6s states of Ce, situated above the empty f band of Ce, is between 5 and 6 eV [8, 42, 43]. Pfau and Schierbaum [42] propose that the gap between valence band and conduction band varies slightly if the Ce valence is considered, specifically the initial f state. Moreover, the bands corresponding to low wavelengths may be associated with the quantum confinement effect due to the small size of the particles (Fig. 3a).

The band centered at ~ 3.4 eV meanwhile has been reported by many investigators as the energy associated with the transition between valence and conduction band in ceria [41, 44]. Other authors, looking at the presence of Ce³⁺ in ceria solids, have questioned the attribution of this energy. One of these theories indicated that the energy of 3.4 eV would be associated with electron transition from the ²F_{5/2} of Ce³⁺, to the conduction band [42]. According to the work of Balestrieri et al. [43], the energy of 3.4 eV would be associated with electronic transitions between the partially filled 4f state, created by the isolated Ce³⁺ ions, to the 5d state of Ce that would be between the 4f state and the conduction band of Ce⁴⁺. Finally, the energy of ~ 3.8 eV could be associated, as is proposed by Pfau and Schierbaum [42], with an inter-layer transition (the intershell transition) between Ce4f¹ and Ce5d (i.e. transition ²F + ²D).

As shown in Fig. 3b, there were no appreciable changes when varying the heat treatment conditions of the cerium oxide samples: temperature (Fig. 3b-i) or treatment time (Fig. 3b-ii and b-iii). It has been found for other solids that heat treatments can create defect sites on their surface [45]. This does not seem to be the case of the ceria synthesized in this work, between 500 and 1000 °C (Fig. 3b). The results of Fig. 3b indicate that the surface stoichiometry,

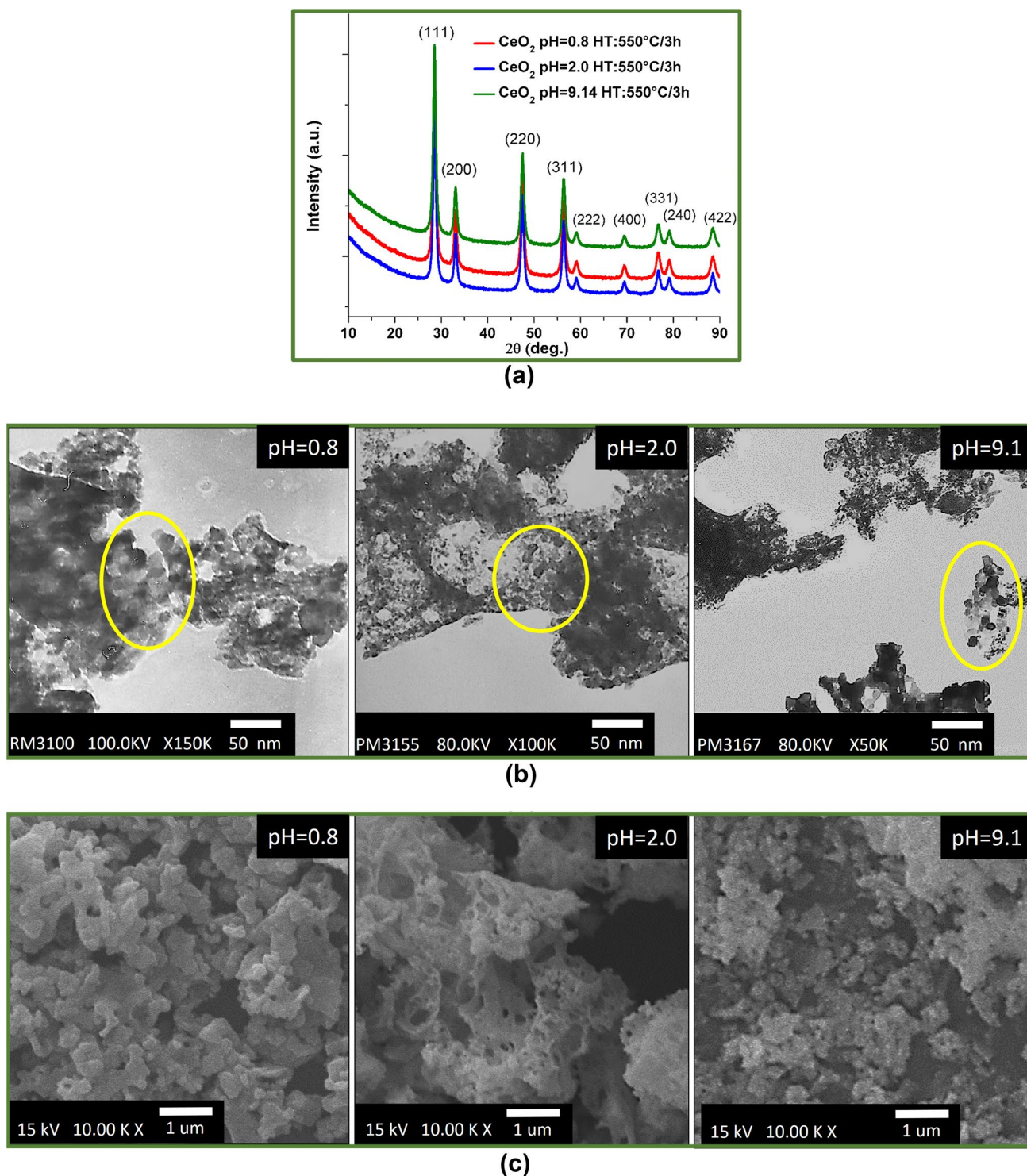


Fig. 2 **a** X-ray diffractograms, **b** TEM and **c** SEM images of CeO₂-NPs synthesized at different pH values and heat treated at 550 °C/3 h

the type of defects and the surface states of the synthesized solids would not be affected, appreciably, by the heat treatment to which they were subjected.

3.2.4 UV–Vis Diffuse Reflectance of Synthesized Cerium Oxide: Gap Energy Values

Figure 3b-i shows the UV–Vis diffuse reflectance spectra (DRS) obtained for CeO₂ samples synthesized at pH ~ 2,

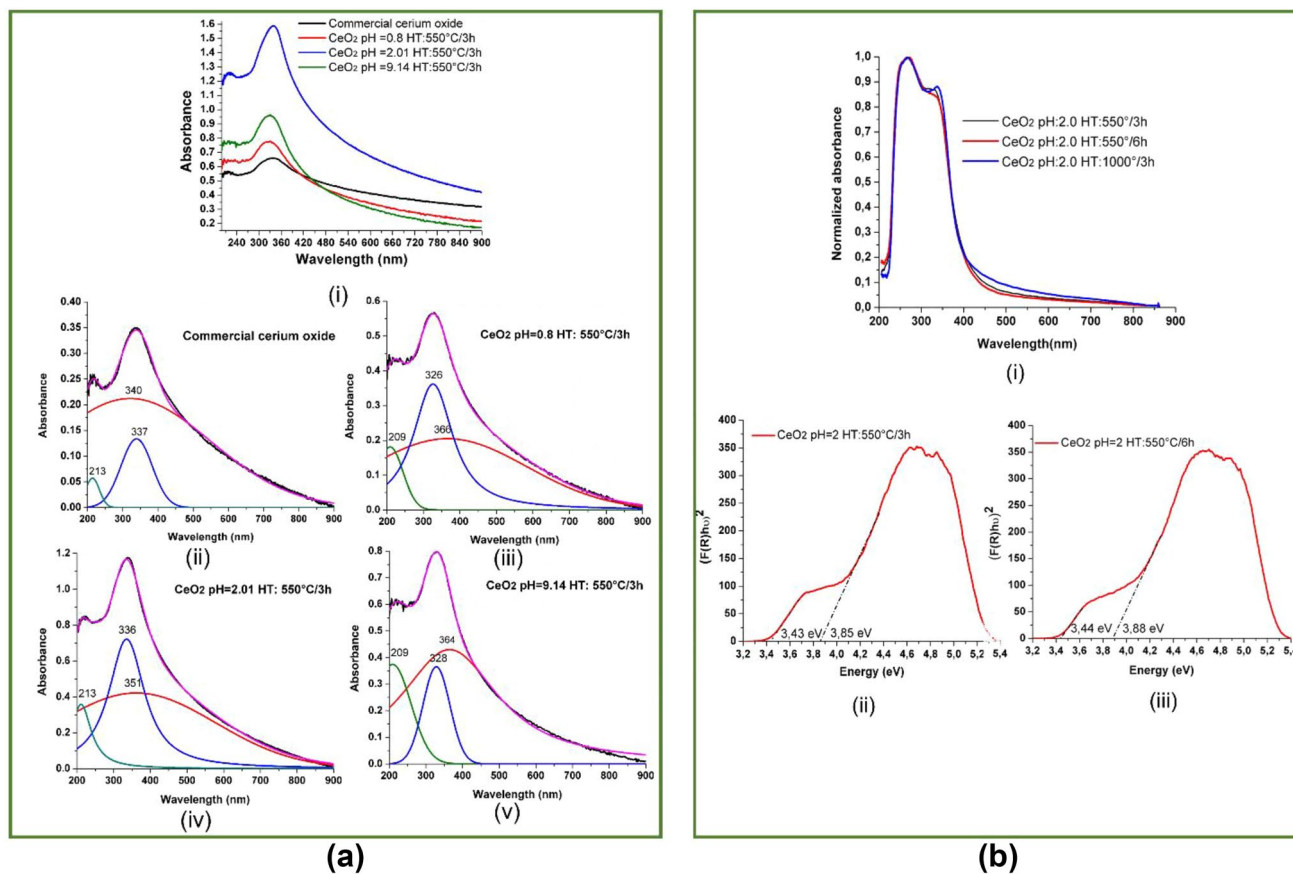


Fig. 3 **a** Absorption spectra in UV–Vis corresponding to commercial cerium oxide and samples synthesized at different pH and heat treated at 550°C/3 h, and deconvolution of the spectra, and **b** diffuse reflectance spectra (DRS) of CeO₂ nanoparticles synthesized at pH 2 and

heat treated at 550 °C, 2 and 6 h, and 1000 °C/3 h (i) and (ii)–(iii) graphics of the Kubelka–Munk transform function as a function of energy

Table 1 Wavelength and energy values related to the principal absorption band observed in the UV–Vis absorption spectra of the different synthesized CeO₂ samples

Sample	Wavelength (nm)	Energy (eV)
Commercial CeO ₂ (SIGMA 99.9%)	213	5.8
	337	3.7
	340	3.6
CeO ₂ pH ~ 1	209	5.9
	326	3.8
	366	3.4
CeO ₂ pH ~ 2	213	5.8
	337	3.7
	351	3.5
CeO ₂ pH ~ 9.1	209	5.9
	328	3.8
	364	3.4

with different heat treatments. These DRS spectra exhibit absorption peaks at 270 and 327 nm and little variation is observed in these. The peaks would be generated by charge

transference from the 2p level of O to the 4f level of Ce and by electronic transition 4f–5d in Ce³⁺.

The UV–Vis diffuse reflectance spectra (Fig. 3b-i) were used to obtain the energy gap value of the CeO₂ samples synthesized at pH ~ 2. For this, the following equation was used [46]:

$$\alpha_b = \frac{B(h\nu - E_g)^n}{h\nu} \quad (2)$$

and making use of the Kubelka–Munk [47] model:

$$[F(R_\infty)h\nu = B(h\nu - E_g)^n] \quad (3)$$

with:

$$F(R_\infty) = \frac{(1 - R_\infty)^2}{2R_\infty}; R_\infty = \frac{R_{\text{Sample}}}{R_{\text{Standard}}} \quad (4)$$

where α_b is the absorption coefficient, $h\nu$ absorbed energy, B absorption constant, E_g energy of the energy gap, $F(R_\infty)$ Kubelka–Munk function, R reflectance and n constant with a value of 1/2 (direct transition) for ceria. The energy of

the incident photon ($h\nu$) and the band gap energy (E_g) are related by the Kubelka–Munk transform function [48], as Eq. 3 indicates. Representing $(\alpha_b h\nu)^2$ or $[F(R\infty)h\nu]^2$ as a function of $h\nu$ (Fig. 3b-ii and b-iii), a straight line can be obtained in the absorption edge, tangential to the curve represented, which on extrapolating to bisect the energy axis, the cut-off point would make it possible to obtain the energy gap value. Figure 3b-ii and b-iii show the gap energy values obtained for the sample synthesized at pH ~ 2 (treated at 550 °C/3 h for 3 and 6 h, respectively). The values obtained were ~ 3.8 eV and ~ 3.4 eV, which show a concordance with the calculations using UV–Vis absorption measurements (Table 1).

3.2.5 Raman Spectroscopy of Synthesized Cerium Oxide

Figure 4a, b show the Raman spectra of the ceria synthesized at different pH values, heat treated at 550 °C/3 h and the commercial sample (SIGMA 99.9%), and Fig. 4c shows the Raman spectra corresponding to ceria subjected to different thermal treatments. These spectra show an intense peak centered at, approximately, 456 cm^{-1} , in which its intensity decreased as pH increased. This peak can be associated with the F_{2g} Raman vibrational mode of the crystalline cubic fluorite type structure of ceria [49, 50], originated by the tension vibrations of the oxygen atoms that surround the cerium [51].

The sample synthesized at pH ~ 9 had a low intensity peak around 560 cm^{-1} (Fig. 4b) that can be associated with the induced defect mode (D). This D band can be attributed to the presence of oxygen vacancies (V_o) due to ceria

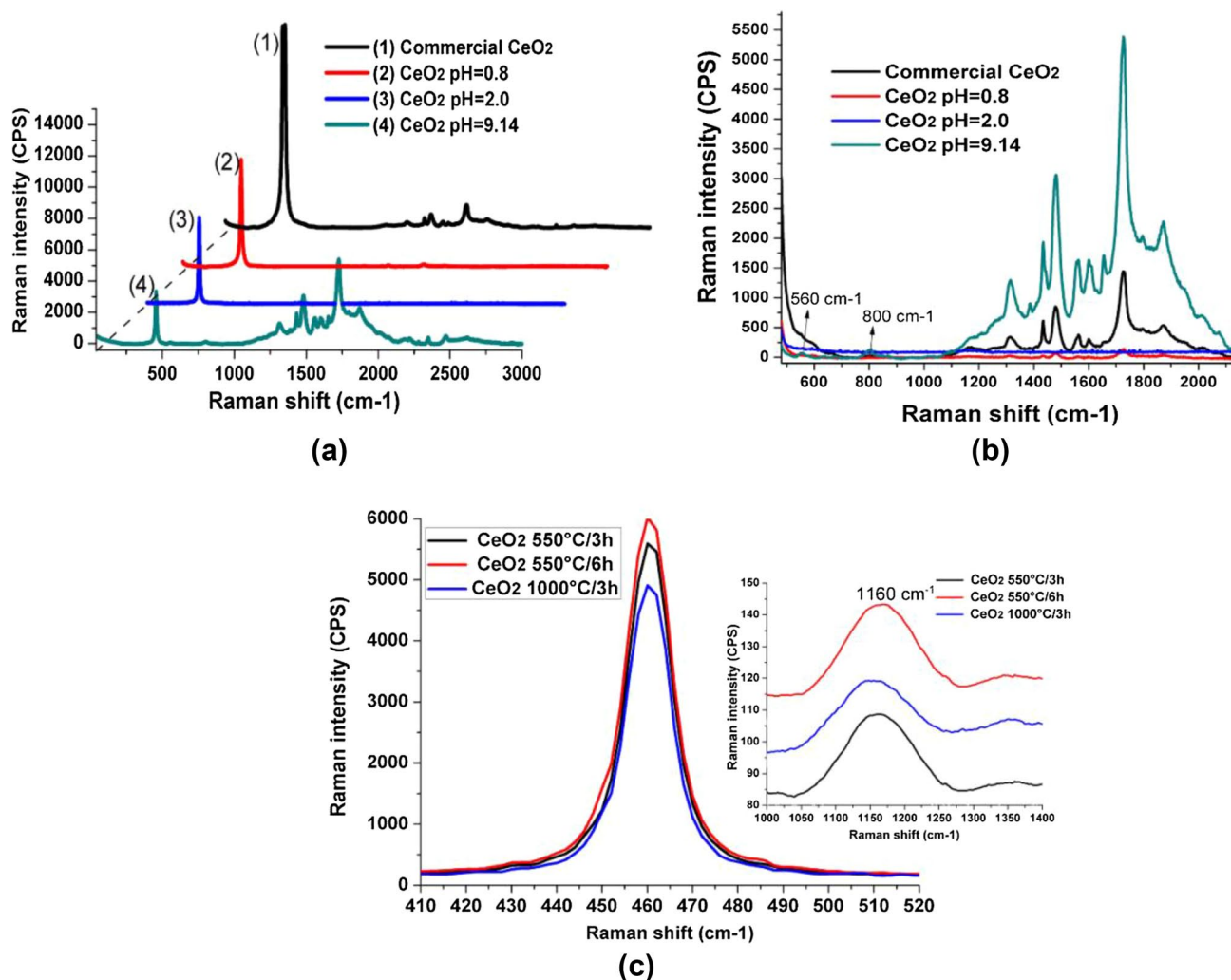


Fig. 4 Raman spectra corresponding to samples synthesized at different pH, treated at 500 °C, (a, b) and at pH 2, treated to different temperatures (c)

reduction [52, 53]. The sample synthesized at basic pH also showed a small band around 800 cm^{-1} (Fig. 4b) that can be attributed to absorbed peroxide species (O_2^{2-}) η^2 and nonplanar bridging peroxo complexes of adsorbed O_2 with two-electron defects in a different local environment [52]. The band located at $\sim 1160\text{ cm}^{-1}$ is observed in all the spectra of Fig. 4, with different intensities (see Fig. 4c), and can be correlated with the Raman mode characteristic of the surface superoxide species (O_2^-) η^1 , giving information about the presence of the oxygen vacancies [49, 52]. In their study, Choi et al. concluded that the partially reduced CeO_2 , on exposure to just 10% oxygen, would show diverse surface species such as side-on, end-on, and non-planar and planar bridging configurations that are characteristic of peroxo and superoxo species [54], species whose characteristic bands are evident in the Raman spectra of the nanoparticles synthesized in this work (Fig. 4). The Raman spectra of the commercial samples and the spectrum obtained at pH ~ 9.1 presented bands at 1315, 1430, 1483, and 1561 cm^{-1} . The bands around 1560 cm^{-1} can be associated with adsorbed molecular oxygen O_2 and the bands that are between 1300 and 1400 cm^{-1} with the absorbed O_2^δ species, with $0 < \delta < 1$. During the synthesis stage of the ceria, for temperatures below $550\text{ }^\circ\text{C}$, the system would contain large amounts of carbon, which would favor a reducing atmosphere and thus the presence of Ce^{3+} in the solid. This Ce^{3+} , on coming into contact with the atmospheric oxygen, would encourage the mechanism proposed by Choi et al. and therefore the presence of peroxo and superoxo species in the ceria. Choi et al. [54] further indicate in their study that the geometry of these configurations would vary according to the reduction of the ceria and the presence of oxygen vacancies.

Besides oxygen, monoxide (CO) and carbon dioxide (CO_2) can be absorbed over the ceria giving rise to new active surface species in the range 1700 – 1800 cm^{-1} (bridged carbonate) and 1430 – 1483 cm^{-1} (unidentate carbonate) [55] as shown in the spectra in Fig. 4a, b.

With the aim of studying the effect of heat treatments on ceria samples synthesized at pH ~ 2 , their Raman spectra were recorded between 410 and 520 cm^{-1} and 1000 – 1400 cm^{-1} , as shown in Fig. 4c. In these spectra little variation is seen in the location and intensity of the band at $\sim 460\text{ cm}^{-1}$ (associated with the symmetric mode of Raman vibration F_{2g}) and 1160 cm^{-1} (characteristic of the surface superoxide species (O_2^-)).

3.2.6 Photoluminescence Spectra

Figure 5 shows the photoluminescence spectra, at room temperature, of the three ceria samples synthesized at different pH values. The spectra underwent a mathematical deconvolution by fitting with Gaussian functions. The positions

of the different emission peaks are almost constant for all samples. The width emission peak of 550 – 900 nm would correspond to the electronic transition of the band gap of CeO_2 . The intensity and the emission bandwidth should give information about the abundance of the defect that exists in the ceria nanoparticles synthesized in this work. Therefore, when there is a high concentration of Ce^{3+} states, and a high concentration of oxygen vacancies, a high percentage of valence electrons can be excited and located in the states that the defects generate in the band gap, or if these defects have electrons (ionized states), these are able to pass to the conduction band, conditions that would lead to a high emission signal [56] being recorded, as is observed in Fig. 5.

The spectra of the sample of interest (Fig. 5) are very similar and consist, mainly, of five emission bands: at $\sim 575\text{ nm}$ (2.15 eV, emission in the yellow), $\sim 600\text{ nm}$ (2.07 eV emission in the orange), $\sim 635\text{ nm}$ (1.96 eV emission in the red), $\sim 698\text{ nm}$ (1.78 eV emission in the red) and $\sim 768\text{ nm}$ (1.62 eV emission in the infrared). These results indicate that the energy states associated with the defects and that are within the energy gap can appreciably affect the optical behavior of the ceria-NPs synthesized in this work, as illustrated in Fig. 5e. These data provided an experimental base in which the presence of ionized states associated with defects in the cerium oxide was consistently found, as is proposed by other systems [57–59], which would be constituted by the energy states that promotes the transitions mentioned above (Fig. 5), and emission in the yellow, orange, red and infrared.

The photoluminescence spectrum of the sample synthesized at pH ~ 2 was recorded using a Xenon laser at a wavelength of 360 nm (3.45 eV) to understand the optical behavior of the synthesized ceria-NPs, and complement prior photoluminescence results considering transitions between bands. The results obtained are shown in Fig. 5d. This spectrum shows one emission band in UV region, 391 nm (3.17 eV), but mainly in the visible region, such as those located at: 417 nm (2.97 eV—violet), 442 nm (2.81 eV—blue), 489 nm (2.54 eV—light blue), 572 nm (2.17 eV—yellow) and 589 nm (2.11 eV—yellow/orange).

The photoluminescence (PL) spectra in Fig. 5 should correspond to recombination processes involving the deeply trapped charge carriers (trap-state PL-TPL) since the bands are wide and are located in the range of longer wavelengths [60, 61]. At room temperature, the TPL band is not detectable for the bulk semiconductors but this can be clearly observed in the case of nanoparticles as a result of the developed and imperfect nanoparticle surface [7]. On the surface, the charge carriers can be located in the surface states such that the lattice imperfections (ion vacancies, dislocations, impurities, etc.) can act as charge traps. The surface of a real nano-crystal is always enriched with several defects, in addition to the dangling bonds, which

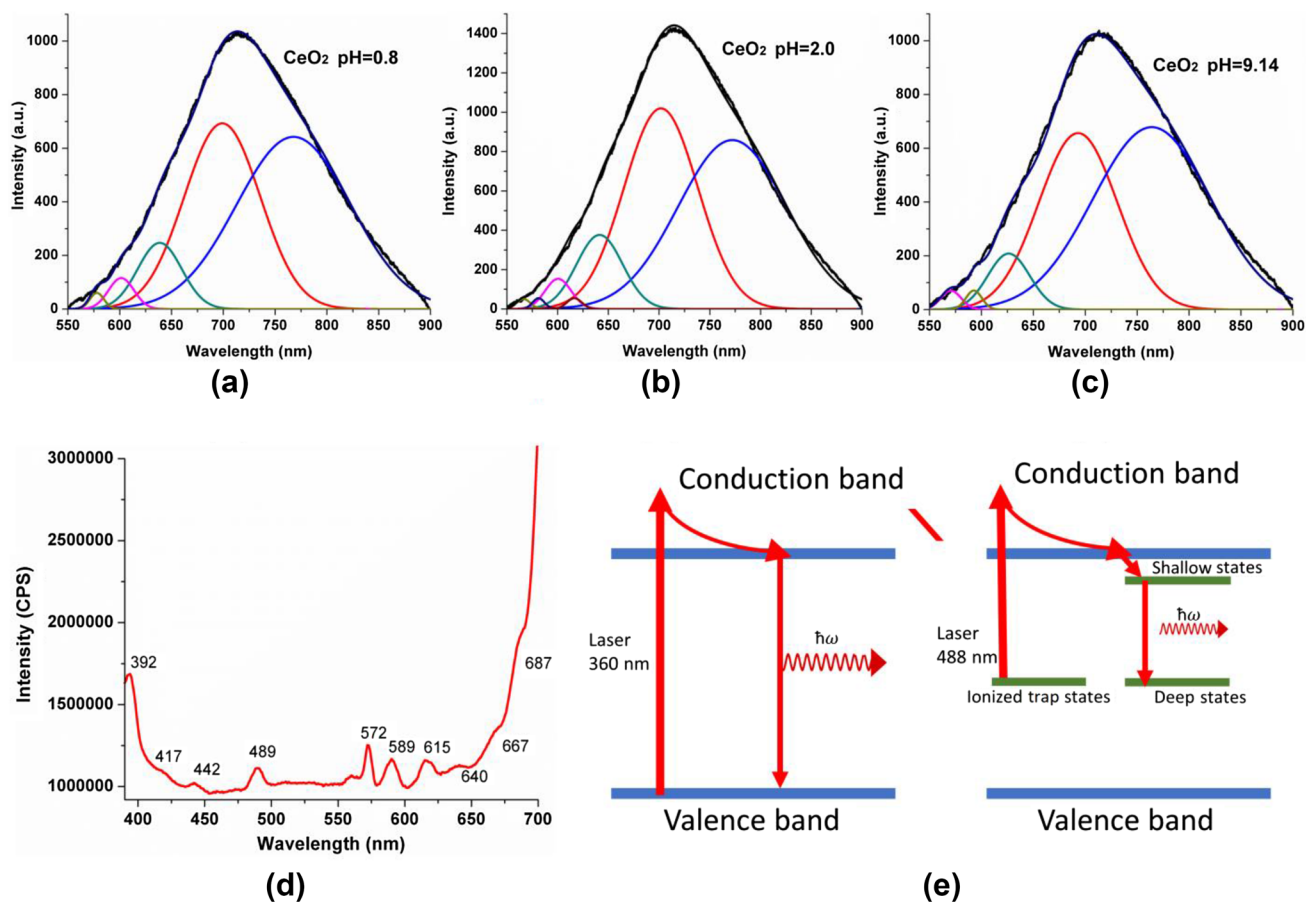


Fig. 5 Photoluminescence spectra of CeO₂ synthesized at **a** pH ~ 1, **b** pH ~ 2, **c** pH 9.14, using an Argon laser (488 nm), **d** photoluminescence spectrum of ceria sample synthesized at pH ~ 2, using Xenon

laser (360 nm), and **e** diagram of the possible radiant electronic transitions taking into consideration the wavelength of the lasers used in the trials. All samples analyzed were heat treated at 550 °C for 3 h

can promote electron–phonon interaction. In Fig. 5e a basic diagram is shown that illustrates the excitation of electrons favored by the laser radiation used (488 nm and 360 nm) as well as the possible trapping processes, considering the Shockley–Read–Hall recombination model [62]. The diagram was structured based on some diagrams proposed in the literature [63–65]. In the diagram (Fig. 5e), the valence band (VB) would be due to the O2p orbitals whereas the conduction band (CB) would be constituted by the Ce5d, 6s orbitals [66] and a narrow sub-band [66] that would be formed by the empty Ce⁴⁺4f⁰ states [67]. Furthermore, although not shown in the diagram, the existence of Ce³⁺ ions in the solid ought to generate another Ce³⁺4f¹ sub-band ~ 1.2–1.5 eV above the VB [67]. Other energy states that could be created within the band gap would be generated by the oxygen vacancies, V_o, which are the most important defects in nanocrystalline ceria [4, 11]. These oxygen defect levels would be found below the Ce⁴⁺4f⁰ sub-band and would be those most responsible for the visible emission peaks observed in the PL spectra in Fig. 5a–d. The oxygen defect levels correspond to vacancies of oxygen without and

with trapped electrons that are normally represented as: F⁰ state (with two trapped electrons), F⁺ state (with a trapped electron) and F⁺⁺ state (without trapped electrons) [68, 69]. Theoretical calculations indicate that the F⁺ states would be closer to the VB than the F⁰ states, at ~ 1.7 eV and ~ 2.1 eV respectively [68, 69], and in the diagram in Fig. 5e they would be represented by the “deep states”. Meanwhile, the F⁺⁺ states would be below the CB, at ~ 2.9–3.0 eV above the Ce³⁺4f¹ sub-band acting as electron traps, and they would not have localized electrons [69]. On the other hand, while the F⁺ and F⁰ states would have electrons and would be partial and fully occupied states, it is possible that they would present empty excited states that are denoted, normally, as F^{++*} and F^{0*}, respectively, and would be close to the CB separated of its fundamental states by 2.4–2.5 eV (F⁺ → F^{++*}) and 2.0–2.1 eV (F⁰ → F^{0*}) [68, 69]. Therefore, the states F⁺⁺, F^{++*} and F^{0*} would be represented in the diagram in Fig. 5e by the “shallow states”. Based on information from the literature [68, 69] and considering the locations of the F states and the Ce³⁺4f¹ subband in the band gap, indicated above, the most prominent bands of the PL spectra in Fig. 5 could

associate with transitions that would involve states: $F^{++} \rightarrow F^+$ (blue/ ~ 442 nm), $F^{+*} \rightarrow F^+$ (light blue/ ~ 489 nm) and $F^{0*} \rightarrow F^0$ (orange/ ~ 600 nm); to the states and subband or band: $F^{++} \rightarrow Ce^{3+}4f^1$ (violet/ ~ 417 nm), $F^+ \rightarrow VB$ (red/ ~ 698 nm) and $F^0 \rightarrow VB$ (yellow/ ~ 575 nm); as well as to the subband and band $Ce^{3+}4f^1 \rightarrow VB$ (infrared/ ~ 768 nm) and to the bands $CB \rightarrow VB$ (UV/ ~ 391 nm). These results indicate that the samples of synthesized ceria had a high concentration of oxygen vacancies that could propitiate an efficient fluorescence, an effect that is established by the percentage of ceria in the Ce^{3+} ionization state. Therefore, the presence in the samples of synthesized CeO_2 -NPs of a high concentration of reduced states of (Ce^{3+}), associated with oxygen vacancies, would generate defect states that could lead to down-conversion emission [70]. It is known that an optical nanomaterial that can emit via either up- or down-conversion is of interest

for new applications in biomedicine, solar cell technology, and gas sensing [70].

3.2.7 X-ray Photoelectron Measurements (XPS)

The sample of CeO_2 -NPs synthesized at pH 9 was examined by X-ray photoelectron spectroscopy (XPS) and the spectrum obtained is shown in Fig. 6. One of the most important characteristics of cerium oxide is the oxidation state of the Ce cation, determinant for the crystal structure of the solid: cubic, fluorite type (CeO_2) for Ce^{4+} , or hexagonal, sesquioxide type (Ce_2O_3), for Ce^{3+} . When the atom forms part of the structure of cerium oxide, the electrons of states $5d^16d^2$ would participate in the bond with the $2p$ valence band of the oxygen [71], while the electron arrangement of $4f^1$ would depend on the associated energy in the electronic

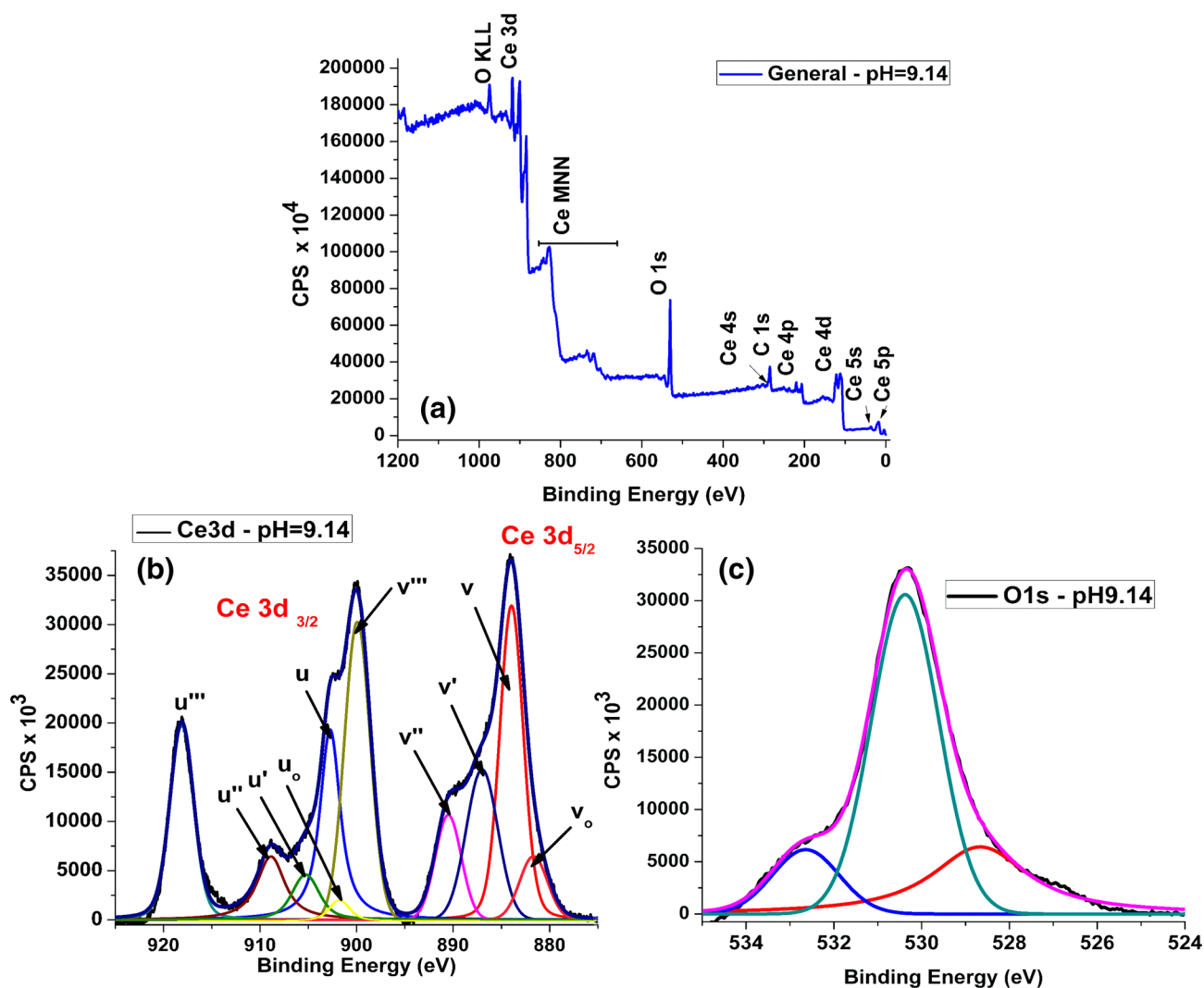


Fig. 6 XPS analysis of CeO_2 -NPs synthesized at pH 9.1: **a** XPS survey-scan of nanoparticles, **b** decomposition of the Ce 3d core level and **c** O 1s level spectra after subtracting a Shirley background

state within the crystal structure as mentioned previously. Due to the strong hybridization of the $2p$ valence band of the oxygen with the Ce $4f$ orbital, quantitative analysis of the reduction of Ce atoms from the $4+$ to the $3+$ state is made extremely difficult [41, 72]. Currently, the most widely used method for determining the Ce oxidation state is measurement of the Ce $3d$ core level using XPS. Figure 6b shows the Ce $3d$ core-level fitted spectra with the corresponding deconvoluted Gaussian–Lorentzian peaks. The observed XPS peaks are attributed to trivalent Ce^{3+} and tetravalent Ce^{4+} . We assigned five pairs of doublets as (u_0, v_0) (u, v), (u', v') , (u'', v'') , and (u''', v''') where u and v come from Ce $3d_{3/2}$ and Ce $3d_{5/2}$ states respectively, according to the convention established by Burroughs et al. [73]. The peaks that can be assigned to Ce^{4+} are: u''' (918.11 eV) and v''' (899.92 eV), which result from the $Ce3d^9 O2p^6 Ce4f^0$ final state; u (902.73 eV) and v (883.95 eV) ($Ce3d^9 O2p^4 Ce4f^2$ final state); u'' (908.87 eV) and v'' (890.50 eV) ($Ce3d^9 O2p^5 Ce4f^1$ final state) [42, 74–76]. The contribution of Ce^{3+} to the Ce $3d$ spectrum consists of two doublet pairs: u_0 (901.00 eV) and v_0 (881.67 eV) ($Ce3d^9 O2p^5 Ce4f^2$ final state), and u' (905.27 eV) and v' (887.00 eV) ($Ce3d^9 O2p^6 Ce4f^1$ final state) [42, 74–76].

Using the components that belong to a definite oxidation state, one can quantify the relative concentrations of the Ce^{3+} and Ce^{4+} ions according to the relations [41]:

$$\%[Ce^{3+}] = \frac{ACe^{+3}}{ACe^{+3} + ACe^{+4}} \times 100 \text{ and } \%[Ce^{4+}] = \frac{ACe^{+4}}{ACe^{+3} + ACe^{+4}} \times 100 \quad (5)$$

where ACe^{+3} and ACe^{+4} denote the total area of the Ce $3d$ peaks for the (III) and (IV) oxidation states, respectively. The calculation shows that the concentration of Ce^{3+} and Ce^{4+} ions in the CeO_2 -NPs were 20.49% and 79.51%, respectively. The trivalent Ce^{3+} can be distributed either in regions of sesquioxide Ce_2O_3 or around O vacancies in the CeO_2 [77].

Figure 6c shows the core level XPS spectrum of O $1s$. The binding energy peak at 530.4 eV may have originated from the oxygen atoms in the lattice [78], and the peak at 532.6 eV may be associated with O^{2-} ions that are in the oxygen-deficient regions with an unusual low coordination [79] and that according to Pfau and Schierbaum [42] would indicate the formation of Ce^{3+} -related surface defects. Regarding the peak located at ~ 528.5 eV, noting the work of Xu et al. [80] and specifically the $1s$ oxygen photoemission spectra, this may correspond to structural O $1s$. This assignment can be explained considering that, while accepting that XPS is a surface technique, the electron escape depth should allow a deep analysis of the nanoceria samples.

The content of O can be calculated supposing that the total oxygen content would be the sum of the O required to

completely oxidize the Ce^{4+} and Ce^{3+} present in the sample, assuming that the Ce^{3+} and the Ce^{4+} form Ce_2O_3 and CeO_2 specifically. The O required to completely oxidize all the cerium ions (the “ x ” parameter in the stoichiometric formula CeO_x) is determined using the formula [75, 76]:

$$x = \frac{[O]}{[Ce]} = \frac{3}{2}[Ce^{3+}] + 2[Ce^{4+}] \quad (6)$$

taking into account that $x = [O]/[Ce]$ is equal to 2 for CeO_2 and 1.5 for Ce_2O_3 and where $[Ce] = [Ce^{4+}] + [Ce^{3+}]$, an amount that can be derived from the XPS analysis. The stoichiometry of oxygen obtained in this study was 1.90 per atom of Ce. The reduction of CeO_2 to $CeO_{2-\gamma}$ ($\gamma = 2 - x$) is caused by the oxygen atoms that become detached from the crystal network, generating oxygen vacancies and producing the reduction of the adjacent ions: from Ce(IV) to Ce(III). The oxygen vacancies and the Ce(III) ions formed would lend a high reactivity to the synthesized CeO_2 -NPs.

4 Conclusions

In the course of this work, a reproducible and reliable method of synthesizing ceria nanoparticles at low temperatures was structured. The results obtained from the characterization of the CeO_2 synthesized indicate that the powder

would contain nanoparticles (< 100 nm). In addition, from the results of both UV–Vis absorption and diffuse reflectance spectroscopy two energy values were obtained that may correspond to the band-gap value (3.8 eV) and the other may be related to the presence of ionized states associated with the defects (of 3.4 eV), mainly of the oxygen vacancies, and isolated Ce^{3+} atoms in the structure of ceria-NPs. Photoluminescence spectra reaffirmed the existence of located states in the gap that led to emissions in the UV and visible: blue, green, yellow, orange, and red, to infrared. Considering the results obtained in the absorption tests in the UV–Vis, diffuse reflectance, Raman, XPS and PL, performed on the samples of synthesized CeO_2 , the partial reduction of cerium ions is evident. This can lead to a high concentration of Ce^{3+} states and oxygen vacancies, with the corresponding introduction of energy levels in the gap. The results obtained from these studies indicate that the states located within the gap are ionized, favoring the passage of electrons to the conduction band, a condition that would propitiate a high emission signal. Moreover, the concentration of oxygen vacancies in the ceria would determine its fluorescence efficient, an effect that is established by the percentage of ceria in

the Ce^{3+} ionization state. This indicates that the conversion Ce^{4+} a Ce^{3+} would fix the efficiency of the ceria if it were to be used as a phosphorous material in solid-state lighting. Specifically, controlling the Ce^{3+} ionization state and the corresponding concentration of oxygen vacancies, one could consider the potential application of the CeO_2 -NPs in bioimaging as the fluorescent wavelength of ceria is in the visible wavelength range.

In conclusion, using the modified polymer complex method, it was possible to synthesize CeO_2 -NPs in a controlled and reproducible way. These nanoparticles presented interesting structural and optical characteristics, specifically an electronic structure with a high concentration of Ce^{3+} states and oxygen vacancies, which generated energy levels in the gap, as indicated by the optical characterization tests. These characteristics would favor potential applications of CeO_2 -NPs in biomedicine, solar cell technology, and gas sensing. As the properties of the nanoparticles are determined mainly by the synthesis method used, other processes of obtaining them should be evaluated to determine if they can obtain CeO_2 -NPs with the characteristics of those synthesized in this work.

Acknowledgements This project was funded through project ID 4162, a Young Researcher agreement with COLCIENCIAS. We are grateful to the University of Cauca for making their laboratory facilities available for carrying out this work, to VRI-Unicauca for all logistical support and to the Surface Science Laboratory of the Industrial University of Santander for their valuable collaboration in the XPS measurements. We are especially grateful to Colin McLachlan for suggestions relating to the English text. To structure the diagram in Fig. 1, icons created by Freepik were used from <http://www.flaticon.com>.

References

- S. Gangopadhyay, D.D. Frolov, A.E. Masunov, S. Seal, J. Alloys Compd. **584**, 199 (2014)
- C. Sun, L. Hong, L. Chen, Energy Environ. Sci. **5**, 8475 (2012)
- N.V. Skorodumova, S.I. Simak, B.I. Lundqvist, I.A. Abrikosov, B. Johansson, Phys. Rev. Lett. **89**, 166601 (2002)
- F. Esch, S. Fabris, L. Zhou, T. Montini, C. Africh, P. Fornasiero, G. Comelli, R. Rosei, Science **309**, 752 (2005)
- N.J. Lawrence, J.R. Brewer, L. Wang, T.S. Wu, J. Wells-Kingsbury, M.M. Ibragimov, G. Wang, Y.L. Soo, W.N. Mei, C.L. Cheung, Nano Lett. **11**, 2666 (2011)
- S. Hull, S.T. Norberg, I. Ahmed, S.G. Eriksson, D. Marrocchelli, P.A. Madden, J. Solid State Chem. **182**, 2815 (2009)
- S.V. Gaponenko, *Optical Properties of Semiconductor Nanocrystals* (Cambridge University Press, Cambridge, 1998)
- N.V. Skorodumova, R. Ahuja, S.I. Simak, I.A. Abrikosov, B. Johansson, B.I. Lundqvist, Phys. Rev. B **64**, 115108 (2001)
- L. Fangxin, W. Chengyun, S. Qingde, Z. Tianpeng, Z. Guiwen, Appl. Opt. **36**, 2796 (1997)
- A.S. Nikolic, M. Boskovic, M. Fabian, D.K. Bozanic, M. Vucinic-Vasic, A. Kremenovic, B. Antic, J. Nanosci. Nanotechnol. **13**, 6787 (2013)
- J. Paier, C. Penschke, J. Sauer, Chem. Rev. **113**, 3949 (2013)
- A. Trovarelli, P. Fornasiero, *Catalysis by Ceria and Related Materials*, 2nd edn. (Imperial College Press—Catalytic Science Series, Italy, 2005)
- Z. Wu, S.H. Overbury, *Catalysis by Materials with Well-Defined Structures* (Elsevier, Oxford, 2015)
- G.A. Deluga, J.R. Salge, L.D. Schmidt, X.E. Verykios, Science **303**, 993 (2004)
- K. Otsuka, T. Ushiyama, I. Yamanaka, Chem. Lett. **22**, 1517 (1993)
- S. Park, J.M. Vohs, R.J. Gorte, Nature **404**, 265 (2000)
- S. Tsunekawa, R. Sivamohan, T. Ohsuna, H. Takahashi, K. Tohji, Mater. Sci. Forum **315–317**, 439 (1999)
- A.M. Grumezescu, *Nanobiomaterials in Antimicrobial Therapy: Applications of Nanobiomaterials*, 6th ed. (William Andrew is an imprint of Elsevier, 2016)
- S. Das, J.M. Dowding, K.E. Klump, J.F. McGinnis, W. Self, S. Seal, Nanomedicine **8**, 1483 (2013)
- P. Jasinski, T. Suzuki, H.U. Anderson, Sensors Actuators B **95**, 73 (2003)
- I. Celardo, J.Z. Pedersen, E. Traversa, L. Ghibelli, Nanoscale **3**, 1411 (2011)
- H.R. Pouretedal, A. Kadkhodaie, Chin. J. Catal. **31**, 1328 (2010)
- M. Mogensen, N.M. Sammes, G.A. Tompsett, Solid State Ionics **129**, 63 (2000)
- K.S. Lin, S. Chowdhury, Int. J. Mol. Sci. **11**, 3226 (2010)
- M. Hirano, M. Inagaki, J. Mater. Chem. **10**, 473 (2000)
- F. Charbgo, M. Bin Ahmad, M. Darroudi, Int. J. Nanomed. **12**, 1401 (2017)
- L. HE, Y. SU, J. Lanhong, S. SHI, J. Rare Earths **33**, 791 (2015)
- C. Sun, L. Chen, Eur. J. Inorg. Chem. **2009**, 3883 (2009)
- I.T. Liu, M.H. Hon, L.G. Teoh, J. Electron. Mater. **42**, 2536 (2013)
- S. Deshpande, S. Patil, S.V. Kuchibhatla, S. Seal, Appl. Phys. Lett. **87**, 133113 (2005)
- Y. Xin, X. Yang, P. Jiang, Z. Zhang, Z. Wang, Y. Zhang, Chem-CatChem **3**, 1772 (2011)
- J.J. Ketzial, A.S. Nesaraj, J. Ceram. Process. Res. **12**, 74 (2011)
- F. Heidari, A. Irankhah, Ceram. Int. **40**, 12655 (2014)
- H.Y. Chang, H.I. Chen, J. Cryst. Growth **283**, 457 (2005)
- V. Morris, P.G. Fleming, J.D. Holmes, M.A. Morris, Chem. Eng. Sci. **91**, 102 (2013)
- D. Zhang, F. Niu, H. Li, L. Shi, J. Fang, Powder Technol. **207**, 35 (2011)
- Q. Yuan, H. Duan, L. Li, L. Sun, Y. Zhang, C. Yan, J. Colloid Interface Sci. **335**, 151 (2009)
- M. Kakihana, J. Ceram. Soc. Japan **1178**, 857 (2009)
- J. Calvache-Muñoz, F.A.F.A. Prado, J. E. Rodríguez-Páez, Colloids Surf. A **529**, 146 (2017)
- K.I. Maslakov, Y.A. Teterin, M.V. Ryzhkov, A.J. Popel, A.Y. Teterin, K.E. Ivanov, S.N. Kalmykov, V.G. Petrov, P.K. Petrov, I. Farnan, Phys. Chem. Chem. Phys. **20**, 16167 (2018)
- L. Truffault, M.-T. Ta, T. Devers, K. Konstantinov, C. Simonard, C. Andreazza, I.P. Nevirkovets, A. Pineau, O. Veron, J.-P. Blondeau, Mater. Res. Bull. **45**, 527 (2010)
- A. Pfau, K.D. Schierbaum, Surf. Sci. **321**, 71 (1994)
- M. Balestrieri, S. Colis, M. Gallart, G. Schmerber, M. Ziegler, P. Gilliot, A. Dinia, J. Mater. Chem. C **3**, 7014 (2015)
- C. Ho, J.C. Yu, T. Kwong, A.C. Mak, S. Lai, Chem. Mater. **17**, 4514 (2005)
- T. Sekiya, T. Yagisawa, N. Kamiya, D. Das Mulmi, S. Kurita, Y. Murakami, T. Kodaira, J. Phys. Soc. Japan **73**, 703 (2004)
- R.A. Smith, *Semiconductors*, 2nd edn. (Cambridge University Press, Cambridge, 1978)
- P. Kubelka, F. Munk, Zeitschrift Für Tech. Phys. **12**, 593 (1931)
- A. Escobedo Morales, E. Sánchez, Mora, U. Pal, Rev. Mex. Física S **53**, 18 (2007)

49. X.H. Lu, X. Huang, S.L. Xie, D.Z. Zheng, Z.Q. Liu, C.L. Liang, Y.X. Tong, *Langmuir* **26**, 7569 (2010)
50. J. Zdravković, B. Simović, A. Golubović, D. Poleti, I. Veljković, M. Šćepanović, G. Branković, *Ceram. Int.* **41**, 1970 (2015)
51. Z.V. Popović, M. Grujić-Brojčin, N. Paunović, M.M. Radonjić, V.D. Araújo, M.I.B. Bernardi, M.M. de Lima, A. Cantarero, *J. Nanoparticle Res.* **17**, 23 (2015)
52. Z. Wu, M. Li, J. Howe, H.M.M. Iii, S.H. Overbury, *Langmuir* **26**, 16595 (2010)
53. T. Taniguchi, T. Watanabe, N. Sugiyama, A.K. Subramani, H. Wagata, N. Matsushita, M. Yoshimura, *J. Phys. Chem. C* **113**, 19789 (2009)
54. Y.M. Choi, H. Abernathy, H.T. Chen, M.C. Lin, M. Liu, *ChemPhysChem* **7**, 1957 (2006)
55. A. Trovarelli, *Catal. Rev.* **38**, 439 (2006)
56. N. Shehata, K. Meehan, M. Hudait, N. Jain, *J. Nanoparticle Res.* **14**, 1173 (2012)
57. C. Lu, G. Li, J. Mao, L. Wang, E.Y. Andrei, *Nano Lett.* **14**, 4628 (2014)
58. H. Yaghoubi, Z. Li, Y. Chen, H.T. Ngo, V.R. Bhethanabotla, B. Joseph, S. Ma, R. Schlaf, A. Takshi, *ACS Catal.* **5**, 327 (2015)
59. P. Tierney, T.J. Ennis, Á Allen, J. Wright, *Thin Solid Films* **603**, 50 (2016)
60. O. Stroyuk, A. Raevskaya, N. Gaponik, O. Selyshchev, V. Dzhan, S. Schulze, D.R.T. Zahn, *J. Phys. Chem. C* **122**, 10267 (2018)
61. S. Biswas, J. Husek, S. Londo, L.R. Baker, *Nano Lett.* **18**, 1228 (2018)
62. W. Shockley, W.T. Read, *Phys. Rev.* **87**, 23 (1952)
63. F. Staub, U. Rau, T. Kirchartz, *ACS Omega* **3**, 8009 (2018)
64. S.K. Kulkarni, *Nanotechnology: Principles and Practices* (Springer, Cham, 2015)
65. U.I. Gaya, *Heterogeneous Photocatalysis Using Inorganic Semiconductor Solids* (Springer, Dordrecht, 2014)
66. D.A. Andersson, S.I. Simak, B. Johansson, I.A. Abrikosov, N.V. Skorodumova, *Phys. Rev. B* **75**, 035109 (2007)
67. M.A. Henderson, C.L. Perkins, M.H. Engelhard, S. Thevuthasan, C.H.F. Peden, *Surf. Sci.* **526**, 1 (2003)
68. S. Tiwari, G. Rathore, N. Patra, A.K. Yadav, D. Bhattacharya, S.N. Jha, C.M. Tseng, S.W. Liu, S. Biring, S. Sen, arXiv:1807.02417v1 (2018)
69. S. Aškračić, Z.D. Dohčević-Mitrović, V.D. Araújo, G. Ionita, M.M. de Lima, A. Cantarero, *J. Phys. D* **46**, 495306 (2013)
70. N. Shehata, K. Meehan, I. Hassounah, M. Hudait, N. Jain, M. Clavel, S. Elhelw, N. Madi, *Nanoscale Res. Lett.* **9**, 231 (2014)
71. E. Shoko, M.F. Smith, R.H. McKenzie, *Phys. Rev. B* **79**, 134108 (2009)
72. K.I. Maslakov, Y.A. Teterin, A.J. Popel, A.Y. Teterin, K.E. Ivanov, S.N. Kalmykov, V.G. Petrov, P.K. Petrov, I. Farnan, *Appl. Surf. Sci.* **448**, 154 (2018)
73. P. Burroughs, A. Hamnett, A.F. Orchard, G. Thornton, *J. Chem. Soc. Dalt. Trans.* **0**, 1686 (1976)
74. D. Mullins, S. Overbury, D. Huntley, *Surf. Sci.* **409**, 307 (1998)
75. P. Patsalas, S. Logothetidis, L. Sygellou, S. Kennou, *Phys. Rev. B* **68**, 1 (2003)
76. N.K. Renuka, *J. Alloys Compd.* **513**, 230 (2012)
77. F. Marabelli, P. Wachter, *Phys. Rev. B* **36**, 1238 (1987)
78. A. Younis, D. Chu, S. Li, *J. Phys. D: Appl. Phys.* **45**, (2012)
79. J. Holgado, G. Munuera, J. Espinós, A. González-Elipé, *Appl. Surf. Sci.* **158**, 164 (2000)
80. J. Xu, J. Harmer, G. Li, T. Chapman, P. Collier, S. Longworth, S.C. Tsang, *Chem. Commun.* **46**, 1887 (2010)

Publisher's Note Springer Nature remains neutral with regard to jurisdictional claims in published maps and institutional affiliations.